

pubs.acs.org/JACS Article

Compression of Organic Molecules Coupled with Hydrogen Bonding Extends the Charge Carrier Lifetime in BA₂Snl₄

Xinbo Ma, Wei-Hai Fang, Run Long,* and Oleg V. Prezhdo



Cite This: J. Am. Chem. Soc. 2024, 146, 16314–16323



Read Online

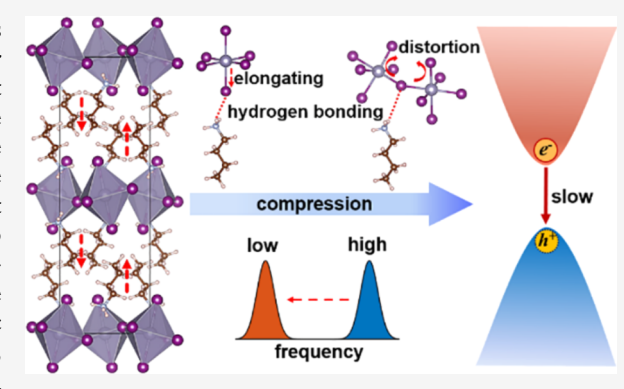
ACCESS I

III Metrics & More

Article Recommendations

Supporting Information

ABSTRACT: Two-dimensional (2D) metal halide perovskites, such as BA_2SnI_4 ($BA=CH_3(CH_2)_3NH_3$), exhibit an enhanced charge carrier lifetime in experiments under strain. Experiments suggest that significant compression of the BA molecule, rather than of the inorganic lattice, contributes to this enhancement. To elucidate the underlying physical mechanism, we apply a moderate compressive strain to the entire system and subsequently introduce significant compression to the BA molecules. We then perform ab initio nonadiabatic molecular dynamics simulations of nonradiative electron—hole recombination. We observe that the overall lattice compression reduces atomic motions and decreases nonadiabatic coupling, thereby delaying electron—hole recombination. Additionally, compression of the BA molecules enhances hydrogen bonding between



the BA molecules and iodine atoms, which lengthens the Sn–I bonds, distorts the $[SnI_6]^{4-}$ octahedra, and suppresses atomic motions further, thus reducing nonadiabatic coupling. Also, the elongated Sn–I bonds and weakened antibonding interactions increase the band gap. Altogether, the compression delays the nonradiative electron–hole recombination by more than a factor of 3. Our simulations provide new and valuable physical insights into how compressive strain, accommodated primarily by the organic ligands, positively influences the optoelectronic properties of 2D layered halide perovskites, offering a promising pathway for further performance improvements.

1. INTRODUCTION

Perovskite solar cells and other devices have received strong interest throughout the past decade. The energy conversion efficiency of perovskite solar cells has risen remarkably quickly, from 3.8% in 2009¹ to 26.1% in 2023.² Metal halide perovskites possess a suitable band gap,³ superior carrier mobility,⁴ and intense optical absorption.⁵ They are defecttolerant⁶ and exhibit effective exciton dissociation into charge carriers. However, their susceptibility to heat and moisture 8, and the toxicity of lead 10 have hindered the widespread application and commercialization. To address these issues, scientists have designed two-dimensional (2D) perovskites that contain large organic molecules within the octahedral frame. 2D Ruddlesden-Popper (RP) and Dion-Jacobson (DJ) phase perovskites have attracted considerable attention and are regarded as alternatives to three-dimensional (3D) perovskites, since they still have excellent optoelectronic properties, while they are more stable and less toxic. 11 The general formulas of the RP and DJ phase perovskites are A'2An-1BnX3n+1 and $A'A_{n-1}B_nX_{3n+1}$, respectively. A' and A represent organic cations, B denotes a metal, X stands for a halide, and n corresponds to the number of inorganic octahedra across each 2D layer. 12 At the same time, the large band gap and low carrier mobility across layers limit the optoelectronic

conversion efficiency compared to the conventional 3D organic—inorganic MAPbI₃ (MA=CH₃NH₃) perovskite. 13

Extensive experimental efforts have been dedicated to increase the optoelectronic conversion efficiency of 2D halide perovskites. 11,13,14 Our previous theoretical work has provided insights into various aspects of the performance of 2D layered halide perovskites, including the spontaneous charge localization between layers, the influence of edges on charge carrier separation and recombination, and the optimization of the spacer cations. 15–19 Significant attention has been given to RP-phase 2D halide perovskites. 20,21 Replacing Pb with Sn to reduce toxicity in 2D perovskites has been considered. 22,23 Strain engineering is a well-known physical tool to tune semiconductors, and it has been used to modulate 2D perovskite optoelectronic properties. 24,25 Strain can be generated by heterogeneous crystallization, 26,27 lattice thermal expansion mismatch, 28,29 and stress induced by light, temper-

Received: April 15, 2024 Revised: May 22, 2024 Accepted: May 23, 2024 Published: May 30, 2024





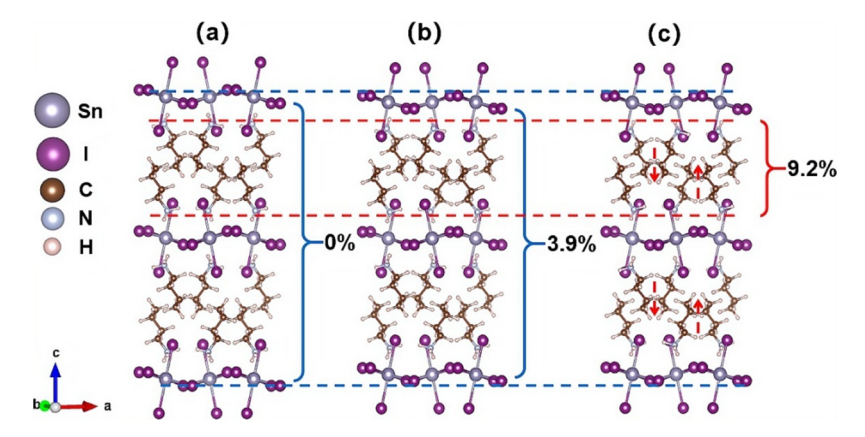


Figure 1. Optimized structures of (a) BASI, (b) LC-BASI, and (c) MC-BASI. The brackets marked with percentages indicate the compression applied. The red arrows in (c) indicate the direction of compression of the BA ligand layers.

ature, external pressure, and electric field.^{30–33} Metal halide perovskites are soft³⁴ and, as a result, are particularly sensitive to strain.

Recent research has highlighted the significance of strain engineering in organic-inorganic perovskites, with particular emphasis on its impact on optoelectronic properties, including band gap, carrier transport, defect properties, and charge losses. 29,35-38 It has been observed that a controlled strain can yield beneficial effects for perovskite device performance. Reports suggest that even slight levels of strain can positively impact the properties of these materials, indicating the potential for strategic strain application to enhance performance. 28,35,36,39-42 Our previous theoretical work has demonstrated that applying compressive and tensile strain to CH3NH3PbI3 can eliminate charge recombination centers formed by defect states by shifting the traps from the band gap into the bands. 43 Further, the influence of strain on 2D halide perovskites has been investigated, particularly in the presence of large organic molecular spacers. Weak van der Waals bonding between spacers in the organic layers in RP perovskites reduces out-of-plane lattice stiffness, leading to intriguing strain effects in these materials.⁴⁴ Recent advancements in the development of 2D tin halide superlattice solar cells have also shed light on the crucial role of the response of organic molecules to strain. 45 Experimental results indicate that a large amplitude compression of organic molecules within the superlattice significantly retards electron-hole recombination, thus enhancing the overall optoelectronic conversion efficiency.⁴⁵ The experimental reports motivate theoretical research into the mechanisms underlying the observed phenomena. A comprehensive atomistic-level understanding of the interplay between strain and carrier dynamics can provide important insights and unlock new possibilities for optimization of 2D layered halide perovskite materials for diverse optoelectronic applications.

To fill the gap between the experimental data and atomistic theoretical analysis, we employ real-time time-dependent density functional theory (TDDFT)^{46,47} and nonadiabatic (NA) molecular dynamics (MD)⁴⁸ to study the nonradiative electron—hole recombination in 2D (BA)₂SnI₄ subject to compressive strain, in particular, focusing on the effect on the strain on BA molecules and their interaction with the inorganic lattice. We demonstrate that a large compressive strain of the organic molecule influences the structure of the inorganic lattice, elongating Sn–I bonds and distorting [SnI₆]^{4–}

octahedra, due to enhanced hydrogen bonding between BA molecules and I atoms. As a result, the BA $_2$ SnI $_4$ layers become more structurally disordered, and the NA coupling between the highest occupied molecular orbital (HOMO) and the lowest unoccupied molecular orbital (LUMO) is reduced. Additionally, the distortion of the $[{\rm SnI}_6]^{4-}$ octahedra weakens their interactions and increases the energy band gap. Combined, these effects significantly, by a factor of 3.4, slow down the recombination of charge carriers. The results are consistent with the experiment and provide valuable insights into the interplay between the strain of organic molecules and carrier dynamics in 2D halide perovskites, suggesting novel strategies for further enhancement of their optoelectronic performance.

2. SIMULATION METHODS

The NA-MD^{48,49} simulations are performed with the decoherenceinduced surface hopping (DISH) method, 50 which is implemented within the time-dependent Kohn-Sham density functional theory. 46,47 The lighter and faster electrons are described quantum mechanically, while the heavier and slower nuclei are treated semiclassically. DISH takes into account the quantum decoherence of the electronic subsystem, giving rise to trajectory branching. 50 The decoherence time scale is estimated as the pure dephasing time of the optical response theory. 51,52 Quantum transitions take place in the DISH algorithm as a result of the decoherence process and take place at decoherence effects, establishing the physical foundation for hops. 50,53,54 This methodology has been successfully applied to investigate photoexcitation dynamics in various systems, including semiconducting quantum dots,⁵⁵ plasmonic nanoparticles,^{56,57} black phosphorus,^{58,59} transition metal dichalcogenides,^{60–62} graphitic phosphorus, 58,59 transition metal dichalcogenides, 60-62 graphitic carbon nitride, 63 2D layered halide perovskites, 15-18 3D organic inorganic perovskites and their interfacial or grain boundary systems, ^{17,64–75} single-atom catalysts, ⁷⁶ ordered magnetic systems, ⁷⁷

All computations are performed utilizing DFT implemented within the Vienna Ab initio Simulation Package (VASP). The projector-augmented wave (PAW) method is employed to describe core electrons. The exchange-correlation functional developed by Perdew, Burke, and Ernzerhof (PBE) is used. The convergence criteria for the total energy change during the electronic structure convergence and force on each atom during geometry optimization are set to 10^{-5} eV and 0.001 eV Å $^{-1}$, respectively. A Γ -centered 6 × 6 × 1 Monkhorst–Pack k-point mesh and 400 eV plane wave energy cutoff are used. The van der Waals interactions are described using the Grimme DFT-D3 method. The geometries of the 156-atom (BA)₂SnI₄ systems are optimized, and the systems are heated to 300 K by repeated velocity rescaling. Subsequently, 4 ps adiabatic MD trajectories are generated within the microcanonical ensemble with a

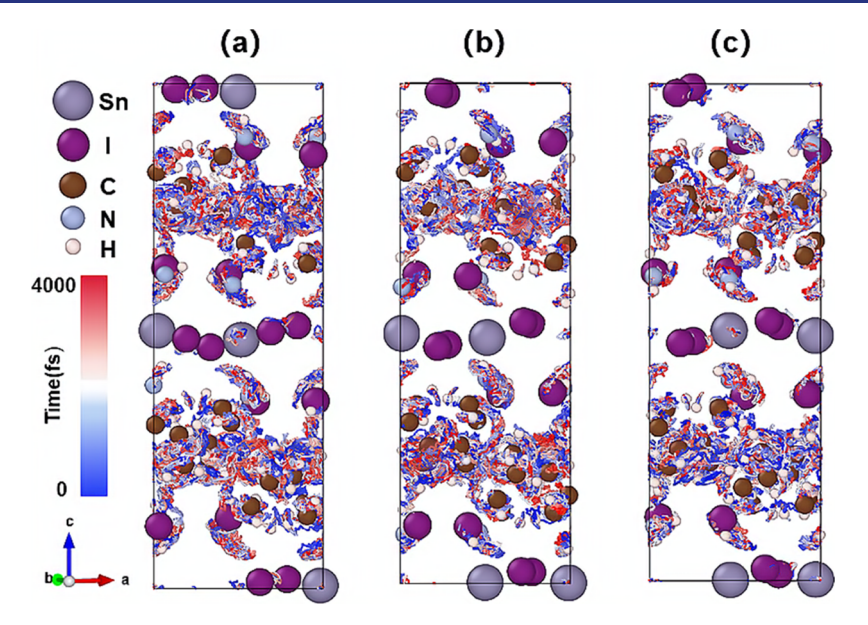


Figure 2. Overlaid images representing the motion during the 4 ps trajectories for (a) BASI, (b) LC-BASI, and (c) MC-BASI. The plots show multiple images of the same system over the 4 ps trajectory, with the change of color representing the time evolution.

1 fs time step, and the NA couplings responsible for electron—hole recombination are computed. The NA Hamiltonians sampled by the 4 ps trajectories are iterated multiple times in order to model the long charge recombination dynamics. All the 4000 geometries from the 4 ps trajectories are chosen as initial conditions for the NA-MD simulations performed using the PYXAID software package. 52,54

3. RESULTS AND DISCUSSION

3.1. Geometric Structure. Tin-based 2D RP perovskites, similar to lead-based perovskites, can be considered derivatives of the 3D MASnI₃ perovskite obtained by cleavage along the (110) plane. The formation of the 2D perovskite framework is supported by hydrogen bonding between BA molecules and I atoms. In this study, we select the monolayer (BA)₂SnI₄ (BASI) as the pristine structure to construct compressed models (Figure 1a). We introduce compressive strain of different magnitudes. In the experiments, 45 the lattice of the tin-based 2D RP perovskite is compressed by 8.6% in the direction perpendicular to the 2D layers. The inorganic lattice compresses relatively little, with the majority of the strain accommodated by the organic cations, which undergo a compression of nearly 15%. Therefore, we first apply a moderate compressive strain of 3.9% perpendicular to the 2D layers to the whole lattice (LC-BASI, Figure 1b). Subsequently, we introduce higher levels (9.2%) of compressive strain into the BA molecules (MC-BASI) starting from the LC-BASI structure. Comparing these systems allows us to identify the influence of compression on the charge carrier dynamics stemming from the overall system or just from the ligands. This information can be used to tune the ligands as well as the inorganic lattice, e.g., the number of octahedra in each 2D layer. The compression of the BA molecules is achieved by reducing the distance between two adjacent BA molecules along the vertical direction, as indicated by the red arrows in Figure 1c. To ensure compression of the BA molecules, the carbon atoms connected to the nitrogen atoms are kept fixed (Figure 1c). The percentage (3.9%) of the inorganic lattice compression is calculated as $\frac{\Delta c}{c}$, where c and Δc represent the lattice constant and the change in the lattice constant

perpendicular to the 2D layers, respectively. The percentage (9.2%) of the BA ligand layer compression is calculated as $\frac{\Delta t}{t}$, in which t and Δt represent the thickness of the BA ligand layers and the change in the thickness perpendicular to the 2D layers, respectively.

Figure 1 shows the optimized geometry of the BASI, LC-BASI, and MC-BASI systems. Representative structures extracted from the MD trajectories at room temperature (300 K) are shown in Figure S1. In the optimized structures, the lattice constants of BASI are 8.27, 8.79, and 25.42 Å, respectively, and the average Sn-I bond length is 3.129 Å, consistent with the values in experiments.^{85,86} The average Sn-I bond lengths decrease to 3.115 Å in LC-BASI and increase to 3.139 Å in MC-BASI. The Sn-I bond lengths averaged canonically at 300 K are 3.147, 3.126, and 3.159 Å in BASI, LC-BASI, and MC-BASI, respectively. The bonds are longer than those in the optimized structures. Notably, the Sn-I bond length is increased significantly in MC-BASI, indicating that the inorganic Sn-I layers are rather soft. The elongation of the Sn-I bond is essential to maintain hydrogen bonding between BA molecules and I atoms under BA molecule compression. Such hydrogen bonding supports the Sn-I octahedral framework. To visually represent the compression effects in these systems, the images from the 4 ps trajectories of the three systems (BASI, LC-BASI, and MC-BASI) are overlaid and shown in Figure 2. The BA molecules move more significantly inside the Sn-I framework than the Sn and I atoms, which fluctuate around their equilibrium positions. Despite the relatively large size of the BA molecules, their long and flexible chains and the small size of the C, N, and H atoms allow a more significant movement compared to the Sn and I atoms. The atomic motions are suppressed in the compressed systems (LC-BASI and MC-BASI) compared to those in BASI, as demonstrated quantitatively by the standard deviations and atomic velocities of BA, Sn, and I, summarized in Table 1.

The canonically average standard deviations of the positions of the BA, Sn, and I atoms and their average atomic velocities (\mathring{A}/fs) are shown in Table 1. The canonically average standard

Table 1. Standard Deviations (Å) of the Positions of BA, Sn, and I Atoms and Their Average Atomic Velocities (Å/fs) Shown in the Parentheses in the BASI, LC-BASI, and MC-BASI Systems

	BA	Sn	I
BASI	0.524(0.0375)	0.317(0.0240)	0.355(0.0261)
LC-BASI	0.521(0.0357)	0.299(0.0223)	0.337(0.0247)
MC-BASI	0.462(0.0317)	0.288(0.0211)	0.313(0.0235)

deviations are obtained as $\sigma_i = \sqrt{\langle (r_i - \langle r_i \rangle)^2 \rangle}$, in which r_i is the location of atom i along the adiabatic MD trajectories and the angular brackets represent canonical averaging. Larger standard deviations indicate stronger atomic fluctuations. The canonically average atomic velocities are obtained numerically according to $v_i = \langle \frac{r_{i+1} - r_i}{t_{i+1} - t_i} \rangle$. The calculated atomic velocities are

consistent with the standard deviations. The fluctuations of the BA molecules in LC-BASI are comparable to those in BASI, while the inorganic lattice (Sn and I) fluctuates less under the compression. Compression of BA molecules in MC-BASI decreases the fluctuations of the Sn and I atoms as well. The smaller amplitude atomic motions, particularly of the inorganic Sn–I lattice that supports charge carriers, suggest that the

electron—vibrational coupling should be suppressed by the compression and that the carrier lifetime should increase.

To identify the influence of strain on geometry distortion in these systems, we analyze three structural features, the in-plane (Sn1-I1) and out-of-plane (Sn1-I2) Sn-I bond lengths and the ∠Sn1-I1-Sn2 bond angle, as shown in Figure 3. The inplane Sn1-I1 bond length characterizes relative motions and interaction between Sn and I atoms within the 2D Sn-I layers, and the out-of-plane Sn1-I2 bond length identifies the stretching motion perpendicular to the 2D Sn-I layers. The ∠Sn1-I1-Sn2 bond angle reflects the distortion and relative orientation of the [SnI₆]⁴⁻ octahedra. The electronic properties and electron-vibrational interactions are influenced by these geometry deformations. The distributions of the in-plane and out-of-plane Sn-I bond lengths are narrower in LC-BASI than that in pristine BASI, indicating reduced bond length fluctuations under lattice compression. The distribution of the in-plane Sn1-I1 bond is broader in MC-BASI, indicating increased bond fluctuations under BA molecule compression. Notably, both in-plane and out-of-plane Sn-I bond lengths increase in MC-BASI under compression of BA molecules compared to pristine BASI, attributed to the hydrogen bonding between BA molecules and I atoms. The distribution of the ∠Sn1−I1−Sn2 angle is narrower in LC-BASI than in pristine

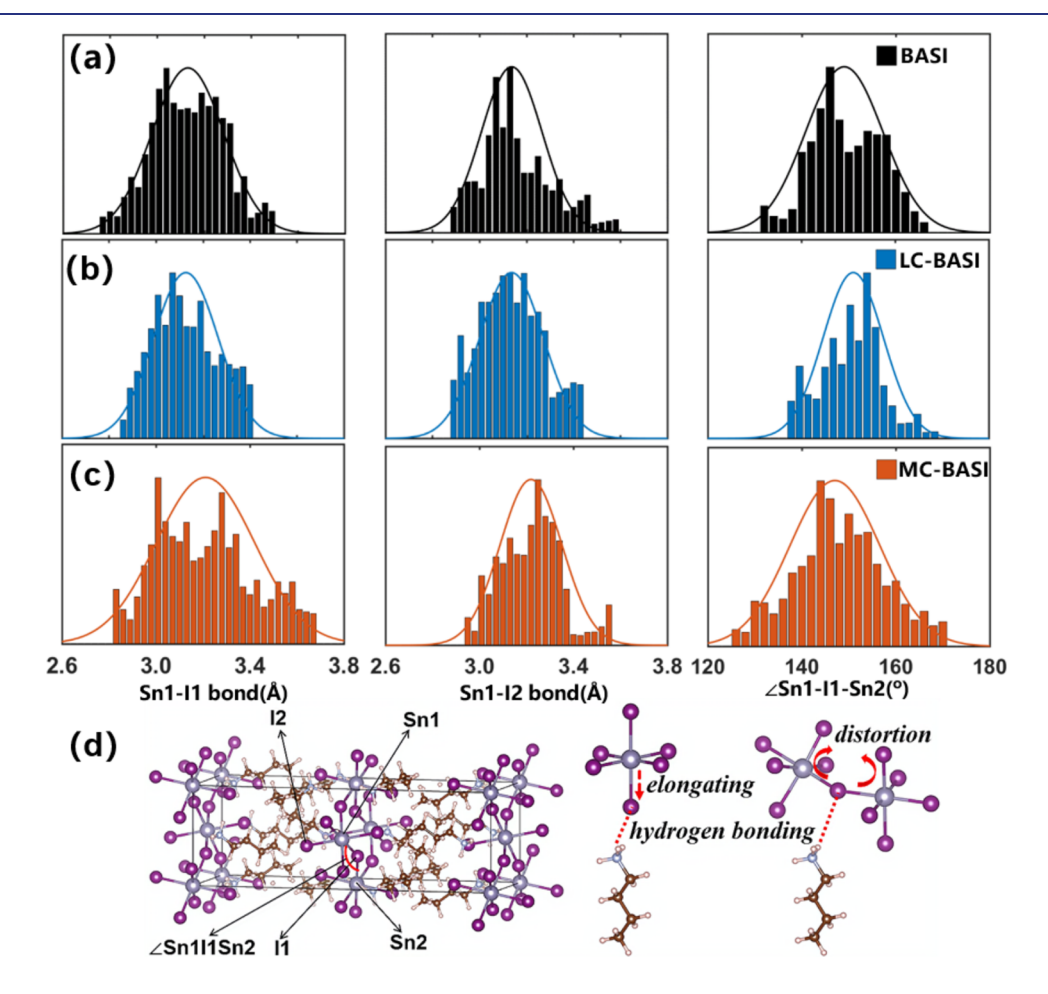


Figure 3. Distributions of the in-plane Sn1–I1 bond length, the out-of-plane Sn1–I2 bond length, and the ∠Sn1–I1–Sn2 angle in (a) BASI, (b) LC-BASI, and (c) MC-BASI systems. (d) Atom labeling and hydrogen bonding between a BA molecule and an I atom. The in-plane Sn1–I1 bond and the out-of-plane Sn1–I2 bond of the 2D layers both elongate in MC-BASI due to hydrogen bonding between BA molecules and I atoms. The longer in-plane Sn1–I1 bond and the larger fluctuation of the ∠Sn1–I1–Sn2 angle indicate an enhanced distortion of $[SnI_6]^{4-}$ octahedra in MC-BASI.

BASI, and the canonically average ∠Sn1-I1-Sn2 angle increases from 149.17° (BASI) to 149.76° (LC-BASI). When BA molecules are compressed in MC-BASI, the distribution of the ∠Sn1-I1-Sn2 angle is significantly broadened and the canonically average ∠Sn1-I1-Sn2 angle decreases notably from 149.17° (BASI) to 146.41° (MC-BASI), signifying larger distortion and fluctuations of $[SnI_6]^{4-}$ octahedra. This can be attributed to the hydrogen bonding interaction between BA molecules and I atoms, which pulls the I atoms from [SnI₆]⁴⁻ octahedra to the molecules (Figure 3d). The in-plane Sn-I bond length increases and the [SnI₆]⁴⁻ octahedra become more distorted (Figure 3d). Structural disorder enhances charge localization and has a considerable impact on electron hole and electron-vibrational interactions, with larger disorder generally giving rise to longer charge carrier lifetimes.^{87,88} The corresponding root-mean-square (RMS) values are also calculated to quantitatively characterize the magnitude of fluctuations for these three structural features. As shown in Table 2, the Sn-I bond lengths are considerably larger, while

Table 2. Canonical RMS Values of the In-Plane Sn1-I1 Bond Length, the Out-of-Plane Sn1-I2 Bond Length, and the ∠Sn1-I1-Sn2 Angle of BASI, LC-BASI, and MC-BASI

	Sn1-I1 (Å)	Sn1-I2 (Å)	Sn1-I1-Sn2 (deg)
BASI	3.148	3.151	149.328
LC-BASI	3.130	3.142	149.896
MC-BASI	3.218	3.164	146.704

the $\angle Sn1-I1-Sn2$ angle is notably smaller in MC-BASI than that in BASI and LC-BASI, further indicating enhanced distortion of $[SnI_6]^{4-}$ octahedra under the BA molecule compression.

3.2. Electronic Structure. Figure 4 shows the projected densities of states (PDOS) of the three systems under investigation. The HOMO is mainly composed of hybridized Sn-5s and I-5p orbitals, while the LUMO is predominantly composed of Sn-5p orbitals, as also seen from the HOMO and LUMO charge densities (Figure S2). The schematic in Figure 4d illustrates the orbital hybridization of the Sn and I atoms. The energy levels of the Sn-5s, Sn-5p, and I-5p orbitals are closely aligned, and their hybridization leads to the formation of the HOMO and LUMO in these systems. The calculated 1.36 eV band gap of optimized BASI is smaller than the

experimental value (1.83 eV)²² because the PBE functional is known to underestimate band gaps.⁸² When the lattice is compressed in optimized LC-BASI, the Sn-I bond length is shortened and the band gap decreases to 1.23 eV. This is attributed to the increased interaction of the Sn and I atomic orbitals, lifting up the valence band edge, i.e., HOMO. When the BA molecules are compressed in optimized MC-BASI, the band gap increases to 1.36 eV. This is due to a stronger distortion of the Sn-I cages, weakening the interaction of [SnI₆]⁴⁻ octahedra. A schematic of the band gap increase due to changes in the orbital hybridization is shown in Figure S3. In these 2D perovskites, the HOMO consists of antibonding combinations of Sn s and I p orbitals. The weaker interaction between [SnI₆]⁴⁻ octahedra reduces the level of the antibonding interaction and lowers the HOMO energy. The LUMO is less responsive to lattice distortions. 89 Consequently, when the lattice is distorted and the interaction weakens in MC-BASI, the HOMO energy decreases and the band gap increases. While the large BA molecules do not directly contribute to the band edges of these systems, their presence induces distortions in the inorganic Sn-I octahedra that support the charge carriers. As a result, the BA cations influence the recombination of charge carriers indirectly, and therefore, charge carrier properties can be tuned by the choice of ligand.

3.3. Electron-Vibrational Interactions. The NA coupling characterizes inelastic electron-vibrational scattering that results in relaxation of the electronic energy to heat and charge losses. The NA coupling matrix element is defined as $-i\hbar\langle\phi_{j}|\nabla_{\!R}|\phi_{k}\rangle\cdot\frac{dR}{dt}$, consisting of the dot product of the electronic matrix element and atomic velocity. The matrix element depends on the relative localization of the electronic wave functions and reflects the sensitivity of the wave functions to atomic displacements. The evolution of the overlap of the HOMO-LUMO charge densities, i.e., wave functions squared, over the 4 ps trajectories is depicted in Figure S4. The canonically averaged HOMO-LUMO charge density overlap decreases in the order LC-BASI (0.0071) > MC-BASI (0.0050) > BASI (0.0048). Typically, a smaller electron hole overlap leads to a weaker NA coupling. However, HOMO-LUMO overlap cannot explain the observed trend of the NA coupling. Therefore, the magnitude of NA coupling is determined by the atomic velocity, reflected in the atomic

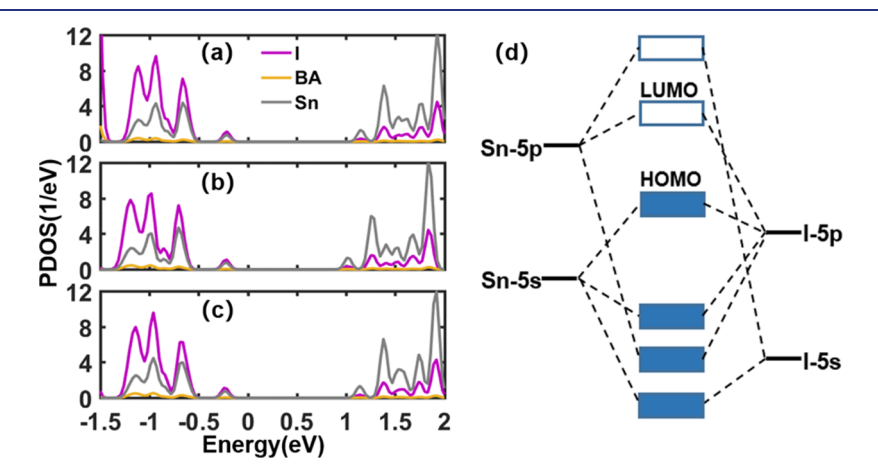


Figure 4. Projected densities of states (PDOS) of (a) BASI, (b) LC-BASI, and (c) MC-BASI. (d) Schematic of hybridization of Sn and I atomic orbitals.

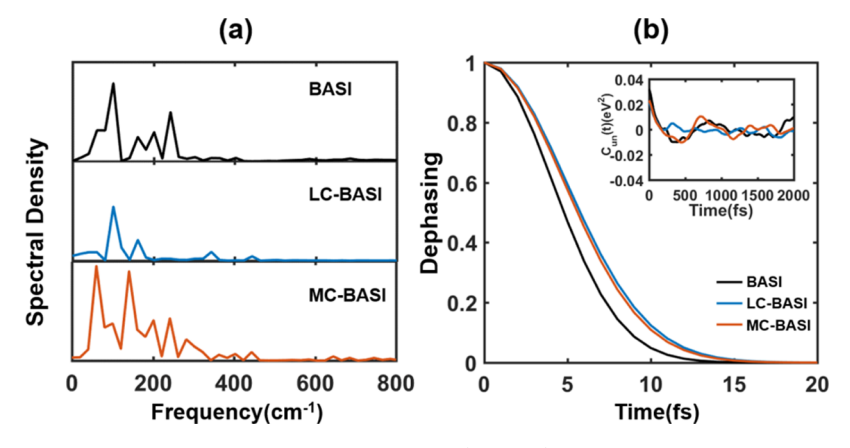


Figure 5. (a) Fourier transforms of un-normalized autocorrelation functions (un-ACF) for fluctuations of the HOMO-LUMO band gaps and (b) pure dephasing functions for the HOMO-LUMO transition in BASI, LC-BASI, and MC-BASI. The inset of (b) shows the un-ACF. A larger initial value of un-ACF generally leads to a shorter pure dephasing time, Table 3.

Table 3. Canonically Averaged Scaled Band Gaps, Pure Dephasing Times, Averaged Absolute NA Coupling, RMS Values of NA Coupling, and Recombination Times for BASI, LC-BASI, and MC-BASI^a

	gap (eV)	dephasing (fs)	NA coupling (meV)	NA coupling RMS (meV)	recombination (ns)
BASI	1.83(1.27)	4.07	1.82	3.99	0.49
LC-BASI	1.72(1.16)	4.90	1.55	2.50	0.72
MC-BASI	1.90(1.34)	4.76	1.45	2.43	1.67

^aThe calculated canonically averaged band gap of BASI is scaled to match the experimental value. The same scaling constant is applied to scale the band gaps of LC-BASI and MC-BASI. The original band gaps are included in parentheses.

velocities reported in Table 1 and correlated with the standard deviations of the atomic positions. The RMS values of the NA coupling are significantly smaller in the compressed systems, especially for MC-BASI, compared to pristine BASI due to the smaller atomic velocity in these systems (Table 1). A smaller NA coupling results in slower charge carrier recombination.

To analyze the phonon modes coupled to the electronic transition, we report spectral densities, computed by Fourier transforms of un-normalized autocorrelation functions (un-ACF) of band gap fluctuations along the MD trajectories, in Figure 5a. Vibrations with frequencies below 300 cm⁻¹ participate in the nonradiative recombination in BASI. Specifically, the Raman-active 100 cm⁻¹ mode is attributed to Sn–I stretching motions^{90,91} and the 60 cm⁻¹ mode arises from Sn–I–Sn bending that causes distortion of [SnI₆]^{4–} octahedra. 92 The higher frequency modes around 200 and 400 cm⁻¹ stem from torsional and wagging motions of BA molecules, respectively.⁹³ In LC-BASI, the signals arising from the high-frequency vibrations above 200 cm⁻¹ decrease significantly, attributed to the overall contraction of the system that enhances the interaction between the BA molecules and the Sn-I framework. In turn, the interaction suppresses the torsional and wagging motions of the BA molecules. The signal arising from the low-frequency vibration around 60 cm⁻¹ is notably smaller in LC-BASI relative to that in BASI and MC-BASI. This can be attributed to the compression of the overall system, suppressing low-frequency bending motions that distort [SnI₆]⁴⁻ octahedra of the 2D perovskite. Conversely, in MC-BASI, the signals arising from the low-frequency vibrations around 60 and 100 cm⁻¹ increase significantly because the BA ligands are compressed away from the inorganic layers, allowing the layers to move more freely. This leads to an enhanced distortion of the [SnI₆]⁴⁻ octahedra and causes partial charge localization, thereby decreasing the NA coupling. Simultaneously, strong hydrogen bonding between BA molecules and I atoms triggers the twisting and wagging motions of the BA molecules in MC-BASI, activating the higher frequency vibrations between 200 and 400 cm⁻¹.

In addition to inelastic electron–vibrational scattering, characterized by NA coupling, elastic scattering causes a loss of coherence in the electronic subsystem. The electronic decoherence time can be evaluated as the pure dephasing time of the optical response theory utilizing the second-order cumulant approximation 51,94

$$D_{ij}(t) = \exp\left(-\frac{1}{\hbar^2} \int_0^t \mathrm{d}t' \int_0^{t'} \mathrm{d}t'' C_{ij}(t'')\right)$$

where $C_{ij}(t)$ is the un-ACF of the phonon-induced fluctuation of the band gap $\delta E_{ij}(t)$ between electronic states i and j, defined as

$$C_{ii}(t) = \langle \delta E_{ii}(t') \delta E_{ii}(t-t') \rangle_{t'}$$

Figure 5b presents the pure dephasing functions. The un-ACFs are shown in the inset, and their initial values represent the square of the band gap fluctuation. The pure dephasing times are derived by fitting the data to a Gaussian, exp $[-0.5(-t/\tau)^2]$. The sub-5 fs pure dephasing times (Table 3) stem from the strong electron-vibrational interaction and the participation of multiple phonon modes. These values are significantly smaller than the electron-hole recombination times,²² necessitating the integration of decoherence into NA-MD simulation. 50,54,95 In general, the values of the pure dephasing time can be rationalized by the initial amplitude and decay characteristics of the un-ACF. 94,96 A larger un-ACF initial value results in a shorter pure dephasing time. The square root of the un-ACF initial value, $\delta^2 E_{ii}(0)$, represents band gap fluctuation, as seen in Figure S5. The calculated band gap variances corroborate the un-ACF initial values, which decrease in the sequence LC-BASI < MC-BASI < BASI. The

pure dephasing times decrease in the opposite order as expected, 94,96 Table 3. The suppression of decoherence/pure dephasing in the compressed system is attributed to a reduction in atomic motions. Faster decoherence often leads to slower carrier recombination.9

3.4. Nonradiative Electron-Hole Recombination. Figure 6 shows the evolution of the population of the first

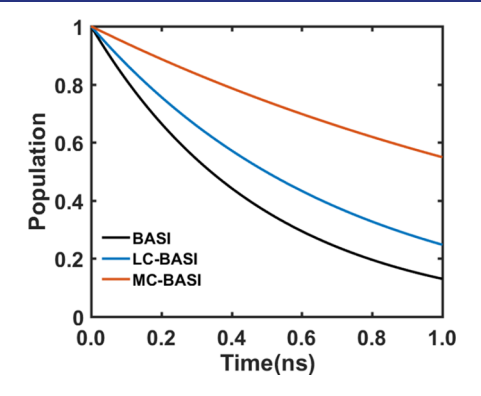


Figure 6. Electron-hole recombination dynamics in BASI, LC-BASI, and MC-BASI.

excited state of the three systems. To account for the underestimation of the band gap by the PBE functional, we scaled the canonically averaged band gap of BASI (1.27 eV) to match the experimental value of 1.83 eV.²² The same constant was applied to shift the canonically averaged band gaps of LC-BASI (1.16 eV) and MC-BASI (1.34 eV), as shown in Table 3. The NA coupling was scaled accordingly to reflect the inverse proportionality to the energy gap. 52 By fitting the data to the exponential function $P(t) = \exp(-t/\tau)$, we obtained the electron-hole recombination time scales, τ , as summarized in Table 3. The calculated electron-hole recombination time of BASI is 0.49 ns, which is consistent with the experimental value.²² When the lattice is compressed by 3.9% in LC-BASI, the electron-hole recombination becomes slower, 0.72 ns. When further compression is applied to the BA molecules, electron-hole recombination becomes even slower, 1.67 ns. Slower carrier recombination results in reduced energy and charge losses and enhanced optoelectronic performance. The interplay among the NA coupling, the pure dephasing time, and the band gap can rationalize the differences in the calculated electron-hole recombination time scales. Specifically, this time scale extends by a factor of 1.5 for LC-BASI and 3.4 for MC-BASI compared to BASI. This extension is due to the reduced NA coupling in LC-BASI. For MC-BASI, both the reduced NA coupling and increased band gap favor a longer carrier lifetime. The pure dephasing times can have a complex influence on the relaxation time. 95 The reported results indicate that the substantial compression of the organic molecules, rather than compression of the inorganic lattice, is the main cause of the extended carrier lifetime in the 2D halide perovskites, rationalizing the experiment.⁴⁵

4. CONCLUSIONS

By performing the ab initio quantum dynamics simulations of nonradiative electron-hole recombination in pristine and compressed 2D layered tin RP halide perovskites, we have demonstrated that the significantly extended charge carrier lifetime in BA₂SnI₄ stems from the notably compressed BA molecules rather than the inorganic lattice compression.

Compression of the inorganic lattice only delays the nonradiative electron-hole recombination by a factor of 1.4 compared to the pristine system due to the suppressed atomic motions and reduced NA coupling. BA molecules undergo much larger compression, and their distortion changes the properties of the inorganic lattice. In particular, the large compression of BA molecules leads to elongating of the Sn-I bonds and enhances distortion of the [SnI₆]⁴⁻ octahedra due to increased strength of hydrogen bonding between the BA molecules and the I atoms of the lattice. This further reduces atomic motions, reduces the NA coupling, and broadens the band gap, thereby delaying the nonradiative electron-hole recombination by a factor of 3.4 relative to the pristine system. The findings shed light on the crucial role of organic molecule compressive strain in extending the lifetime of charge carriers, offering essential mechanistic insights into charge carrier recombination and providing a new strategy to improve the optoelectronic properties of 2D halide perovskites.

ASSOCIATED CONTENT

Supporting Information

The Supporting Information is available free of charge at https://pubs.acs.org/doi/10.1021/jacs.4c05191.

Structures at 0 and 300 K, HOMO and LUMO charge densities, schematic of hybridization of Sn and I atomic orbitals, evolutions of the overlap between HOMO and LUMO charge densities, and HOMO-LUMO gap at 300 K (PDF)

AUTHOR INFORMATION

Corresponding Author

Run Long - College of Chemistry, Key Laboratory of Theoretical & Computational Photochemistry of Ministry of Education, Beijing Normal University, Beijing 100875, P. R. China; orcid.org/0000-0003-3912-8899; Email: runlong@bnu.edu.cn

Authors

Xinbo Ma - College of Chemistry, Key Laboratory of Theoretical & Computational Photochemistry of Ministry of Education, Beijing Normal University, Beijing 100875, P. R.

Wei-Hai Fang - College of Chemistry, Key Laboratory of Theoretical & Computational Photochemistry of Ministry of Education, Beijing Normal University, Beijing 100875, P. R. China; orcid.org/0000-0002-1668-465X

Oleg V. Prezhdo - University of Southern California, Los Angeles, California 90007, United States; oorcid.org/ 0000-0002-5140-7500

Complete contact information is available at: https://pubs.acs.org/10.1021/jacs.4c05191

The authors declare no competing financial interest.

ACKNOWLEDGMENTS

This work was supported by the National Natural Science Foundation of China (grant nos. 92372121 and 22288201). R.L. acknowledges the Fundamental Research Funds for the Central Universities. O.V.P. acknowledges the support of the US National Science Foundation (grant no. CHE-2154367).

REFERENCES

- (1) Kojima, A.; Teshima, K.; Shirai, Y.; Miyasaka, T. Organometal Halide Perovskites as Visible-Light Sensitizers for Photovoltaic Cells. *J. Am. Chem. Soc.* **2009**, *131* (17), 6050–6051.
- (2) Park, J.; Kim, J.; Yun, H.-S.; Paik, M. J.; Noh, E.; Mun, H. J.; Kim, M. G.; Shin, T. J.; Seok, S. I. Controlled Growth of Perovskite Layers with Volatile Alkylammonium Chlorides. *Nature* **2023**, *616*, 724–730.
- (3) Yin, W. J.; Shi, T.; Yan, Y. Unique Properties of Halide Perovskites as Possible Origins of the Superior Solar Cell Performance. *Adv. Mater.* **2014**, *26*, 4653–4658.
- (4) Ponseca, C. S.; Savenije, T. J.; Abdellah, M.; Zheng, K. B.; Yartsev, A.; Pascher, T.; Harlang, T.; Chabera, P.; Pullerits, T.; Stepanov, A.; et al. Organometal Halide Perovskite Solar Cell Materials Rationalized: Ultrafast Charge Generation, High and Microsecond-Long Balanced Mobilities, and Slow Recombination. *J. Am. Chem. Soc.* 2014, 136, 5189–5192.
- (5) De Wolf, S.; Holovsky, J.; Moon, S. J.; Loper, P.; Niesen, B.; Ledinsky, M.; Haug, F. J.; Yum, J. H.; Ballif, C. Organometallic Halide Perovskites: Sharp Optical Absorption Edge and Its Relation to Photovoltaic Performance. *J. Phys. Chem. Lett.* **2014**, *5*, 1035–1039.
- (6) Agiorgousis, M. L.; Sun, Y. Y.; Zeng, H.; Zhang, S. Strong Covalency-Induced Recombination Centers in Perovskite Solar Cell Material CH₃NH₃PbI₃. *J. Am. Chem. Soc.* **2014**, *136*, 14570–14575.
- (7) Ghosh, T.; Aharon, S.; Etgar, L.; Ruhman, S. Free Carrier Emergence and Onset of Electron–Phonon Coupling in Methylammonium Lead Halide Perovskite Films. *J. Am. Chem. Soc.* **2017**, 139, 18262–18270.
- (8) Conings, B.; Drijkoningen, J.; Gauquelin, N.; Babayigit, A.; D'Haen, J.; D'Olieslaeger, L.; Ethirajan, A.; Verbeeck, J.; Manca, J.; Mosconi, E.; et al. Intrinsic Thermal Instability of Methylammonium Lead Trihalide Perovskite. *Adv. Energy Mater.* **2015**, *5*, No. 1500477.
- (9) Hidalgo, J.; Kaiser, W.; An, Y.; Li, R.; Oh, Z.; Castro-Méndez, A.-F.; LaFollette, D. K.; Kim, S.; Lai, B.; Breternitz, J.; et al. Synergistic Role of Water and Oxygen Leads to Degradation in Formamidinium-Based Halide Perovskites. *J. Am. Chem. Soc.* **2023**, *145*, 24549–24557.
- (10) Babayigit, A.; Ethirajan, A.; Muller, M.; Conings, B. Toxicity of Organometal Halide Perovskite Solar Cells. *Nat. Mater.* **2016**, *15*, 247–251.
- (11) Cao, D. H.; Stoumpos, C. C.; Farha, O. K.; Hupp, J. T.; Kanatzidis, M. G. 2D Homologous Perovskites as Light-Absorbing Materials for Solar Cell Applications. *J. Am. Chem. Soc.* **2015**, *137*, 7843–7850.
- (12) Mao, L. L.; Stoumpos, C. C.; Kanatzidis, M. G. Two-Dimensional Hybrid Halide Perovskites: Principles and Promises. *J. Am. Chem. Soc.* **2019**, *141*, 1171–1190.
- (13) Shao, M.; Bie, T.; Yang, L.; Gao, Y.; Jin, X.; He, F.; Zheng, N.; Yu, Y.; Zhang, X. Over 21% Efficiency Stable 2D Perovskite Solar Cells. Adv. Mater. 2022, 34, No. e2107211.
- (14) Zhao, X.; Liu, T.; Loo, Y. L. Advancing 2D Perovskites for Efficient and Stable Solar Cells: Challenges and Opportunities. *Adv. Mater.* **2021**, *34* (3), No. 2105849.
- (15) Zhang, Z.; Fang, W. H.; Tokina, M. V.; Long, R.; Prezhdo, O. V. Rapid Decoherence Suppresses Charge Recombination in Multi-Layer 2D Halide Perovskites: Time-Domain Ab Initio Analysis. *Nano Lett.* **2018**, *18*, 2459–2466.
- (16) Zhang, Z.; Fang, W. H.; Long, R.; Prezhdo, O. V. Exciton Dissociation and Suppressed Charge Recombination at 2D Perovskite Edges: Key Roles of Unsaturated Halide Bonds and Thermal Disorder. J. Am. Chem. Soc. 2019, 141, 15557–15566.
- (17) Shi, R.; Zhang, Z.; Fang, W.-H.; Long, R. Charge localization control of electron—hole recombination in multilayer two-dimensional Dion—Jacobson hybrid perovskites. *J. Mater. Chem. A* **2020**, *8*, 9168—9176.
- (18) Dai, D.; Shi, R.; Long, R. Improving Lattice Rigidity and Charge Carrier Lifetime by Engineering Spacer Cation of Ruddlesden-Popper Perovskites: A Time-Domain Ab Initio Study. *J. Phys. Chem. Lett.* **2022**, *13*, 2718–2724.

- (19) Shi, R.; Long, R.; Fang, W.-H.; Prezhdo, O. V. Rapid Interlayer Charge Separation and Extended Carrier Lifetimes Due to Spontaneous Symmetry Breaking in Organic and Mixed Organic—Inorganic Dion—Jacobson Perovskites. *J. Am. Chem. Soc.* **2023**, *145*, 5297—5309.
- (20) Sidhik, S.; Wang, Y.; De Siena, M.; Asadpour, R.; Torma, A. J.; Terlier, T.; Ho, K.; Li, W.; Puthirath, A. B.; Shuai, X.; et al. Deterministic Fabrication of 3D/2D Perovskite Bilayer Stacks for Durable and Efficient Solar Cells. *Science* **2022**, *377*, 1425–1430.
- (21) Liang, C.; Gu, H.; Xia, Y.; Wang, Z.; Liu, X.; Xia, J.; Zuo, S.; Hu, Y.; Gao, X.; Hui, W.; et al. Two-Dimensional Ruddlesden—Popper Layered Perovskite Solar Cells Based on Phase-Pure Thin Films. *Nat. Energy* **2021**, *6*, 38–45.
- (22) Cao, D. H.; Stoumpos, C. C.; Yokoyama, T.; Logsdon, J. L.; Song, T.-B.; Farha, O. K.; Wasielewski, M. R.; Hupp, J. T.; Kanatzidis, M. G. Thin Films and Solar Cells Based on Semiconducting Two-D i m e n s i o n a l R u d d l e s d e n P o p p e r $(CH_3(CH_2)_3NH_3)_2(CH_3NH_3)_{n-1}Sn_nI_{3n+1}$ Perovskites. ACS Energy Lett. 2017, 2, 982–990.
- (23) Gong, J.; Hao, M.; Zhang, Y.; Liu, M.; Zhou, Y. Layered 2D Halide Perovskites Beyond the Ruddlesden-Popper Phase: Tailored Interlayer Chemistries for High-Performance Solar Cells. *Angew. Chem., Int. Ed.* **2022**, *61*, No. e202112022.
- (24) Hubbard, S. M.; Cress, C. D.; Bailey, C. G.; Raffaelle, R. P.; Bailey, S. G.; Wilt, D. M. Effect of Strain Compensation on Quantum Dot Enhanced Gaas Solar Cells. *Appl. Phys. Lett.* **2008**, 92, No. 123512.
- (25) Ahn, G. H.; Amani, M.; Rasool, H.; Lien, D. H.; Mastandrea, J. P.; Ager Iii, J. W.; Dubey, M.; Chrzan, D. C.; Minor, A. M.; Javey, A. Strain-Engineered Growth of Two-Dimensional Materials. *Nat. Commun.* **2017**, *8*, No. 608.
- (26) Correa-Baena, J. P.; Saliba, M.; Buonassisi, T.; Gratzel, M.; Abate, A.; Tress, W.; Hagfeldt, A. Promises and Challenges of Perovskite Solar Cells. *Science* **2017**, *358*, 739–744.
- (27) Jones, T. W.; Osherov, A.; Alsari, M.; Sponseller, M.; Duck, B. C.; Jung, Y.-K.; Settens, C.; Niroui, F.; Brenes, R.; Stan, C. V.; et al. Lattice Strain Causes Non-Radiative Losses in Halide Perovskites. *Energy Environ. Sci.* **2019**, *12*, 596–606.
- (28) Zhao, J. J.; Deng, Y. H.; Wei, H. T.; Zheng, X. P.; Yu, Z. H.; Shao, Y. C.; Shield, J. E.; Huang, J. S. Strained hybrid perovskite thin films and their impact on the intrinsic stability of perovskite solar cells. *Sci. Adv.* **2017**, *3*, No. eaao5616.
- (29) Rolston, N.; Bush, K. A.; Printz, A. D.; Gold-Parker, A.; Ding, Y.; Toney, M. F.; McGehee, M. D.; Dauskardt, R. H. Engineering Stress in Perovskite Solar Cells to Improve Stability. *Adv. Energy Mater.* **2018**, 8 (29), No. 1802139.
- (30) Azpiroz, J. M.; Mosconi, E.; Bisquert, J.; De Angelis, F. Defect Migration in Methylammonium Lead Iodide and Its Role in Perovskite Solar Cell Operation. *Energy Environ. Sci.* **2015**, *8*, 2118–2127.
- (31) Zhou, Y.; You, L.; Wang, S.; Ku, Z.; Fan, H.; Schmidt, D.; Rusydi, A.; Chang, L.; Wang, L.; Ren, P.; et al. Giant Photostriction in Organic-Inorganic Lead Halide Perovskites. *Nat. Commun.* **2016**, 7, No. 11193.
- (32) Kim, D.; Yun, J. S.; Sharma, P.; Lee, D. S.; Kim, J.; Soufiani, A. M.; Huang, S.; Green, M. A.; Ho-Baillie, A. W. Y.; Seidel, J. Light- and Bias-Induced Structural Variations in Metal Halide Perovskites. *Nat. Commun.* **2019**, *10*, No. 444.
- (33) Khenkin, M. V.; Katz, E. A.; Abate, A.; Bardizza, G.; Berry, J. J.; Brabec, C.; Brunetti, F.; Bulović, V.; Burlingame, Q.; Di Carlo, A.; et al. Consensus statement for stability assessment and reporting for perovskite photovoltaics based on ISOS procedures. *Nat. Energy* **2020**, *5*, 35–49.
- (34) Fu, Y.; Zhu, H.; Chen, J.; Hautzinger, M. P.; Zhu, X. Y.; Jin, S. Metal Halide Perovskite Nanostructures for Optoelectronic Applications and the Study of Physical Properties. *Nat. Rev. Mater.* **2019**, *4*, 169–188.
- (35) Zhu, C.; Niu, X.; Fu, Y.; Li, N.; Hu, C.; Chen, Y.; He, X.; Na, G.; Liu, P.; Zai, H.; et al. Strain Engineering in Perovskite Solar Cells

- and Its Impacts on Carrier Dynamics. Nat. Commun. 2019, 10, No. 815.
- (36) Chen, Y.; Lei, Y.; Li, Y.; Yu, Y.; Cai, J.; Chiu, M. H.; Rao, R.; Gu, Y.; Wang, C.; Choi, W.; et al. Strain Engineering and Epitaxial Stabilization of Halide Perovskites. *Nature* **2020**, *577*, 209–215.
- (37) Zhang, X.; Turiansky, M. E.; Shen, J.-X.; Van de Walle, C. G. Iodine Interstitials as a Cause of Nonradiative Recombination in Hybrid Perovskites. *Phys. Rev. B* **2020**, *101*, No. 140101(R).
- (38) Keeble, D. J.; Wiktor, J.; Pathak, S. K.; Phillips, L. J.; Dickmann, M.; Durose, K.; Snaith, H. J.; Egger, W. Identification of Lead Vacancy Defects in Lead Halide Perovskites. *Nat. Commun.* **2021**, *12*, No. 5566.
- (39) Kong, L.; Liu, G.; Gong, J.; Hu, Q.; Schaller, R. D.; Dera, P.; Zhang, D.; Liu, Z.; Yang, W.; Zhu, K.; et al. Simultaneous Band-Gap Narrowing and Carrier-Lifetime Prolongation of Organic-Inorganic Trihalide Perovskites. *Proc. Natl. Acad. Sci. U.S.A.* **2016**, *113*, 8910–8915
- (40) Boopathi, K. M.; Martín-García, B.; Ray, A.; Pina, J. M.; Marras, S.; Saidaminov, M. I.; Bonaccorso, F.; Di Stasio, F.; Sargent, E. H.; Manna, L.; Abdelhady, A. L. Permanent Lattice Compression of Lead-Halide Perovskite for Persistently Enhanced Optoelectronic Properties. ACS Energy Lett. 2020, 5, 642–649.
- (41) Kim, G.; Min, H.; Lee, K. S.; Lee, D. Y.; Yoon, S. M.; Seok, S. I. Impact of Strain Relaxation on Performance of Alpha-Formamidinium Lead Iodide Perovskite Solar Cells. *Science* **2020**, *370*, 108–112.
- (42) Yang, B.; Bogachuk, D.; Suo, J.; Wagner, L.; Kim, H.; Lim, J.; Hinsch, A.; Boschloo, G.; Nazeeruddin, M. K.; Hagfeldt, A. Strain Effects on Halide Perovskite Solar Cells. *Chem. Soc. Rev.* **2022**, *51*, 7509–7530.
- (43) Qiao, L.; Fang, W. H.; Long, R.; Prezhdo, O. V. Elimination of Charge Recombination Centers in Metal Halide Perovskites by Strain. *J. Am. Chem. Soc.* **2021**, *143*, 9982–9990.
- (44) Fu, J.; Xu, Q.; Abdelwahab, I.; Cai, R.; Febriansyah, B.; Yin, T.; Loh, K. P.; Mathews, N.; Sun, H.; Sum, T. C. Strain Propagation in Layered Two-Dimensional Halide Perovskites. *Sci. Adv.* **2022**, *8*, No. eabq1971.
- (45) Lei, Y.; Li, Y.; Lu, C.; Yan, Q.; Wu, Y.; Babbe, F.; Gong, H.; Zhang, S.; Zhou, J.; Wang, R.; et al. Perovskite Superlattices with Efficient Carrier Dynamics. *Nature* **2022**, *608*, 317–323.
- (46) Craig, C. F.; Duncan, W. R.; Prezhdo, O. V. Trajectory Surface Hopping in the Time-Dependent Kohn-Sham Approach for Electron-Nuclear Dynamics. *Phys. Rev. Lett.* **2005**, *95*, No. 163001.
- (47) Fischer, S. A.; Habenicht, B. F.; Madrid, A. B.; Duncan, W. R.; Prezhdo, O. V. Regarding the Validity of the Time-Dependent Kohn—Sham Approach for Electron-Nuclear Dynamics Via Trajectory Surface Hopping. *J. Chem. Phys.* **2011**, *134*, No. 024102.
- (48) Jasper, A. W.; Nangia, S.; Zhu, C.; Truhlar, D. G. Non-Born—Oppenheimer Molecular Dynamics. *Acc. Chem. Res.* **2006**, 39, 101–108.
- (49) Prezhdo, O. V. Modeling Non-Adiabatic Dynamics in Nanoscale and Condensed Matter Systems. *Acc. Chem. Res.* **2021**, 54, 4239–4249.
- (50) Jaeger, H. M.; Fischer, S.; Prezhdo, O. V. Decoherence-Induced Surface Hopping. *J. Chem. Phys.* **2012**, *137*, No. 22A545.
- (51) Mukamel, S. Principles of Nonlinear Optical Spectroscopy; Oxford University Press, 1995.
- (52) Akimov, A. V.; Prezhdo, O. V. The Pyxaid Program for Non-Adiabatic Molecular Dynamics in Condensed Matter Systems. *J. Chem. Theory Comput.* **2013**, *9*, 4959–4972.
- (53) Prezhdo, O. V. Mean Field Approximation for the Stochastic Schrödinger Equation. *J. Chem. Phys.* **1999**, *111*, 8366–8377.
- (54) Akimov, A. V.; Prezhdo, O. V. Advanced Capabilities of the Pyxaid Program: Integration Schemes, Decoherence Effects, Multiexcitonic States, and Field-Matter Interaction. *J. Chem. Theory Comput.* **2014**, *10*, 789–804.
- (55) Hyeon-Deuk, K.; Prezhdo, O. V. Time-Domain Ab Initio Study of Auger and Phonon-Assisted Auger Processes in a Semiconductor Quantum Dot. *Nano Lett.* **2011**, *11*, 1845–1850.

- (56) Zhang, Z. S.; Liu, L. H.; Fang, W. H.; Long, R.; Tokina, M. V.; Prezhdo, O. V. Plasmon-Mediated Electron Injection from Au Nanorods into MoS₂: Traditional Versus Photoexcitation Mechanism. *Chem* **2018**, *4*, 1112–1127.
- (57) Li, W.; Xue, T.; Mora-Perez, C.; Prezhdo, O. V. Ab initio Quantum Dynamics of Plasmonic Charge Carriers. *Trends Chem.* **2023**, *5*, 634–645.
- (58) Wei, Y. Q.; Long, R. Grain Boundaries Are Benign and Suppress Nonradiative Electron-Hole Recombination in Monolayer Black Phosphorus: A Time-Domain Ab Initio Study. *J. Phys. Chem. Lett.* **2018**, *9*, 3856–3862.
- (59) Zhang, L.; Vasenko, A. S.; Zhao, J.; Prezhdo, O. V. Mono-Elemental Properties of 2D Black Phosphorus Ensure Extended Charge Carrier Lifetimes under Oxidation: Time-Domain Ab Initio Analysis. *J. Phys. Chem. Lett.* **2019**, *10*, 1083–1091.
- (60) Li, L.; Long, R.; Prezhdo, O. V. Why Chemical Vapor Deposition Grown MoS₂ Samples Outperform Physical Vapor Deposition Samples: Time-Domain Ab Initio Analysis. *Nano Lett.* **2018**, *18*, 4008–4014.
- (61) Yang, Y.; Fang, W. H.; Benderskii, A.; Long, R.; Prezhdo, O. V. Strain Controls Charge Carrier Lifetimes in Monolayer WSe₂: Ab Initio Time Domain Analysis. *J. Phys. Chem. Lett.* **2019**, *10*, 7732–7739
- (62) Wang, X.; Long, R. Oxidation Notably Accelerates Nonradiative Electron-Hole Recombination in MoS₂ by Different Mechanisms: Time-Domain Ab Initio Analysis. *J. Phys. Chem. Lett.* **2020**, *11*, 4086–4092.
- (63) Agrawal, S.; Wang, B. P.; Wu, Y. F.; Casanova, D.; Prezhdo, O. V. Photocatalytic Activity of Dual Defect Modified Graphitic Carbon Nitride Is Robust to Tautomerism: Machine Learning Assisted Ab Initio Quantum Dynamics. *Nanoscale* **2024**, *16*, 8986–8995.
- (64) Tong, C.-J.; Li, L.; Liu, L.-M.; Prezhdo, O. V. Synergy between Ion Migration and Charge Carrier Recombination in Metal-Halide Perovskites. *J. Am. Chem. Soc.* **2020**, *142*, 3060–3068.
- (65) Liu, Y.; Long, R.; Fang, W. H.; Prezhdo, O. V. Nuclear Quantum Effects Prolong Charge Carrier Lifetimes in Hybrid Organic-Inorganic Perovskites. J. Am. Chem. Soc. 2023, 145, 14112–14123.
- (66) Qiao, L.; Fang, W. H.; Long, R. The Interplay between Lead Vacancy and Water Rationalizes the Puzzle of Charge Carrier Lifetimes in CH₃NH₃PbI₃: Time-Domain Ab Initio Analysis. *Angew. Chem., Int. Ed.* **2020**, 59, 13347–13353.
- (67) Qiao, L.; Fang, W.-H.; Long, R.; Prezhdo, O. V. Atomic Model for Alkali Metal Passivation of Point Defects at Perovskite Grain Boundaries. ACS Energy Lett. 2020, 5, 3813–3820.
- (68) Zhao, X.; Long, R. Benign Effects of Twin Boundaries on Charge Carrier Lifetime in Metal Halide Perovskites by a Time-Domain Study. *J. Phys. Chem. Lett.* **2021**, *12*, 8575–8582.
- (69) Qiao, L.; Fang, W. H.; Prezhdo, O. V.; Long, R. Suppressing Oxygen-Induced Deterioration of Metal Halide Perovskites by Alkaline Earth Metal Doping: A Quantum Dynamics Study. *J. Am. Chem. Soc.* **2022**, *144*, 5543–5551.
- (70) Liu, D. Y.; Perez, C. M.; Vasenko, A. S.; Prezhdo, O. V. Ag-Bi Charge Redistribution Creates Deep Traps in Defective Cs₂AgBiBr₆: Machine Learning Analysis of Density Functional Theory. *J. Phys. Chem. Lett.* **2022**, *13*, 3645–3651.
- (71) Liu, D. Y.; Wu, Y. F.; Vasenko, A. S.; Prezhdo, O. V. Grain Boundary Sliding and Distortion on a Nanosecond Timescale Induce Trap States in CsPbBr₃: Ab Initio Investigation with Machine Learning Force Field. *Nanoscale* **2022**, *15*, 285–293.
- (72) Prezhdo, O. V.; Wu, Y. F.; Liu, D. Y.; Chu, W. B.; Wang, B. P.; Vasenko, A. S. Fluctuations at Metal Halide Perovskite Grain Boundaries Create Transient Trap States: Machine Learning Assisted Ab Initio Analysis. ACS Appl. Mater. Interfaces 2022, 14, 55753—55761.
- (73) Liu, D. Y.; Wu, Y. F.; Samatov, M. R.; Vasenko, A. S.; Chulkov, E. V.; Prezhdo, O. V. Compression Eliminates Charge Traps by Stabilizing Perovskite Grain Boundary Structures: An Ab Initio

- Analysis with Machine Learning Force Field. Chem. Mater. 2024, 36, 2898–2906.
- (74) Liu, L. H.; Fang, W. H.; Long, R.; Prezhdo, O. V. Lewis Base Passivation of Hybrid Halide Perovskites Slows Electron-Hole Recombination: Time-Domain Ab Lnitio Analysis. *J. Phys. Chem. Lett.* **2018**, *9*, 1164–1171.
- (75) Qiao, L.; Fang, W. H.; Long, R.; Prezhdo, O. V. Extending Carrier Lifetimes in Lead Halide Perovskites with Alkali Metals by Passivating and Eliminating Halide Interstitial Defects. *Angew. Chem., Int. Ed.* **2020**, *59*, 4684–4690.
- (76) Cheng, C.; Fang, W. H.; Long, R.; Prezhdo, O. V. Water Splitting with a Single-Atom Cu/TiO₂ Photocatalyst: Atomistic Origin of High Efficiency and Proposed Enhancement by Spin Selection. *JACS Au* **2021**, *1*, 550–559.
- (77) Zhou, Z. B.; Zheng, Z. F.; He, J. J.; Wang, J. L.; Prezhdo, O. V.; Frauenheim, T. Ultrafast Laser Control of Antiferromagnetic-Ferrimagnetic Switching in Two-Dimensional Ferromagnetic Semiconductor Heterostructures. *Nano Lett.* **2023**, 23, 5688–5695.
- (78) Kresse, G.; Hafner, J. Ab Initio Molecular Dynamics for Liquid Metals. *Phys. Rev. B* **1993**, *47*, 558–561.
- (79) Blöchl, P. E. Projector Augmented-Wave Method. *Phys. Rev. B* **1994**, *50*, 17953–17979.
- (80) Chu, W. B.; Prezhdo, O. V. Concentric Approximation for Fast and Accurate Numerical Evaluation of Nonadiabatic Coupling with Projector Augmented-Wave Pseudopotentials. *J. Phys. Chem. Lett.* **2021**, *12*, 3082–3089.
- (81) Chu, W. B.; Zheng, Q. J.; Akimov, A. V.; Zhao, J.; Saidi, W. A.; Prezhdo, O. V. Accurate Computation of Nonadiabatic Coupling with Projector Augmented-Wave Pseudopotentials. *J. Phys. Chem. Lett.* **2020**, *11*, 10073–10080.
- (82) Perdew, J. P.; Burke, K.; Ernzerhof, M. Generalized Gradient Approximation Made Simple. *Phys. Rev. Lett.* **1996**, *77*, 3865–3868.
- (83) Monkhorst, H. J.; Pack, J. D. Special Points for Brillouin-Zone Integrations. *Phys. Rev. B* **1976**, *13*, 5188–5192.
- (84) Grimme, S. Semiempirical Gga-Type Density Functional Constructed with a Long-Range Dispersion Correction. *J. Comput. Chem.* **2006**, 27, 1787–1799.
- (85) Takahashi, Y.; Obara, R.; Nakagawa, K.; Nakano, M.; Tokita, J.-y.; Inabe, T. Tunable Charge Transport in Soluble Organic—Inorganic Hybrid Semiconductors. *Chem. Mater.* **2007**, *19*, 6312–6316.
- (86) Wong, M. K.; Liu, F.; Kam, C. S.; Leung, T. L.; Tam, H. W.; Djurišić, A. B.; Popović, J.; Li, H.; Shih, K.; Low, K.-H.; et al. Synthesis of Lead-Free Perovskite Films by Combinatorial Evaporation: Fast Processes for Screening Different Precursor Combinations. Chem. Mater. 2017, 29, 9946–9953.
- (87) Munson, K. T.; Kennehan, E. R.; Doucette, G. S.; Asbury, J. B. Dynamic Disorder Dominates Delocalization, Transport, and Recombination in Halide Perovskites. *Chem* **2018**, *4*, 2826–2843.
- (88) Shi, R.; Fang, Q.; Vasenko, A. S.; Long, R.; Fang, W. H.; Prezhdo, O. V. Structural Disorder in Higher-Temperature Phases Increases Charge Carrier Lifetimes in Metal Halide Perovskites. *J. Am. Chem. Soc.* **2022**, *144*, 19137–19149.
- (89) Prasanna, R.; Gold-Parker, A.; Leijtens, T.; Conings, B.; Babayigit, A.; Boyen, H. G.; Toney, M. F.; McGehee, M. D. Band Gap Tuning Via Lattice Contraction and Octahedral Tilting in Perovskite Materials for Photovoltaics. *J. Am. Chem. Soc.* **2017**, *139*, 11117–11124.
- (90) Stoumpos, C. C.; Cao, D. H.; Clark, D. J.; Young, J.; Rondinelli, J. M.; Jang, J. I.; Hupp, J. T.; Kanatzidis, M. G. Ruddlesden–Popper Hybrid Lead Iodide Perovskite 2D Homologous Semiconductors. *Chem. Mater.* **2016**, 28, 2852–2867.
- (91) Kahmann, S.; Duim, H.; Fang, H. H.; Dyksik, M.; Adjokatse, S.; Rivera Medina, M.; Pitaro, M.; Plochocka, P.; Loi, M. A. Photophysics of Two-Dimensional Perovskites—Learning from Metal Halide Substitution. *Adv. Funct. Mater.* **2021**, *31*, No. 2103778.
- (92) Dhanabalan, B.; Leng, Y. C.; Biffi, G.; Lin, M. L.; Tan, P. H.; Infante, I.; Manna, L.; Arciniegas, M. P.; Krahne, R. Directional Anisotropy of the Vibrational Modes in 2D-Layered Perovskites. ACS Nano 2020, 14, 4689–4697.

- (93) Spirito, D.; Asensio, Y.; Hueso, L. E.; Martín-García, B. Raman Spectroscopy in Layered Hybrid Organic-Inorganic Metal Halide Perovskites. *J. Phys. Mater.* **2022**, *5*, No. 034004.
- (94) Akimov, A. V.; Prezhdo, O. V. Persistent Electronic Coherence Despite Rapid Loss of Electron-Nuclear Correlation. *J. Phys. Chem. Lett.* **2013**, *4*, 3857–3864.
- (95) Gumber, S.; Prezhdo, O. V. Zeno and Anti-Zeno Effects in Nonadiabatic Molecular Dynamics. *J. Phys. Chem. Lett.* **2023**, *14*, 7274–7282.
- (96) Madrid, A. B.; Hyeon-Deuk, K.; Habenicht, B. F.; Prezhdo, O. V. Phonon-Induced Dephasing of Excitons in Semiconductor Quantum Dots: Multiple Exciton Generation, Fission, and Luminescence. ACS Nano 2009, 3, 2487–2494.
- (97) Long, R.; Prezhdo, O. V.; Fang, W. Nonadiabatic Charge Dynamics in Novel Solar Cell Materials. *Wiley Interdiscip. Rev.: Comput. Mol. Sci.* **2017**, *7*, No. e1305.